Comp. Part. Mech.
DOI 10.1007/s40571-016-0113-8

Fingering phenomena during grain–grain displacement

Nathália M. P. Mello[1] · Humberto A. Paiva[2] · G. Combe[3] · A. P. F. Atman[2,4,5]

Received: 3 September 2015 / Revised: 4 April 2016 / Accepted: 15 April 2016

Abstract Spontaneous formation of fingered patterns during the displacement of dense granular assemblies was experimentally reported few years ago, in a radial Hele-Shaw cell. Here, by means of discrete element simulations, we have recovered the experimental findings and extended the original study to explore the control parameters space. In particular, using assemblies of grains with different geometries (monodisperse, bidisperse, or polydisperse), we measured the macroscopic stress tensor in the samples in order to confirm some conjectures proposed in analogy with Saffman–Taylor viscous fingering phenomena for immiscible fluids. Considering an axial setup which allows to control the discharge of grains and to follow the trajectory and the pressure gradient along the displacing interface, we have applied the Darcy law for laminar flow in fluids in order to measure an "effective viscosity" for each assembly combination, in an attempt to mimic variation of the viscosity ratio between the injected/displaced fluids in the Saffman–Taylor experiment. The results corroborate the analogy with the viscous fluids displacement, with the bidisperse assembly corresponding to the less viscous geometry. But, differently to fluid case, granular fingers only develop for a specific combination of displaced/injected geometries, and we have demonstrated that it is always related with the formation of a force chain network along the finger direction.

Keywords Fingering phenomena · Granular materials · Molecular dynamics simulation · Effective viscosity

1 Introduction

Granular systems are ubiquitous on human daily activities and natural phenomena, presenting a rich phenomenology with several remarkable features, most of them remaining without a comprehensive theoretical description [5,22,30–32,42]. The capacity of a granular assembly that behaves as a solid, a liquid, or even a gas depending on the external driving is related to the occurrence of metastable states [4,33,41,45], and several studies are devoted to describe the occurrence of these states in different phenomena: avalanches [13,47], jamming/unjamming transition [12,15,35,53], segregation [38,40,44], history dependence [6,16,27], reverse buoyancy [2,28,50], granulence [19,20,46,48], clogging [39,57,58], etc. Among these, the spontaneous pattern formation [17,34,36,40,55] is one of the most intriguing phenomena due its intrinsically out-of-equilibrium nature. Hence, theoretical descriptions treating these systems are seldom found in the literature [49].

Nevertheless, pattern formation is a key concept to understand how nature works and creates forms, and the quest to access the basic knowledge of the underlying mechanisms of a wide range of phenomena is still attracting the inter-

Electronic supplementary material The online version of this article (doi:10.1007/s40571-016-0113-8) contains supplementary material, which is available to authorized users.

✉ A. P. F. Atman
atman@dppg.cefetmg.br

1 Post Graduation Program in Mathematical and Computer Modeling (PPGMMC), Centro Federal de Educação Tecnológica de Minas Gerais (CEFET-MG), Av. Amazonas 7675, Belo Horizonte, CEP 30510-000, Brazil

2 Departamento de Física e Matemática, CEFET-MG, Belo Horizonte, Brazil

3 UJF-Grenoble 1, Grenoble-INP, CNRS UMR 5521, 3SR Lab, 38041 Grenoble, France

4 PPGMMC/CEFET-MG, Belo Horizonte, Brazil

5 National Institute of Science and Tecnology for Complex Systems - INCT-SC, Rio de Janeiro, Brazil

Published online: 10 May 2016

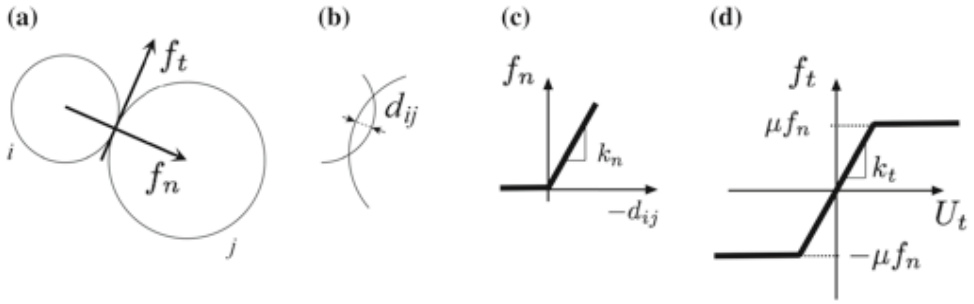

Fig. 1 **a** Normal (n) and tangential (t) directions at the contact point between two grains. **b** Interpenetration d at the contact point. **c** Force law in the normal direction. **d** Force law in tangential direction. *Symbols* are explained in the text

est of researchers from different fields as biology, physics, engineering, computation, etc. [13,54,56]. In particular, the displacement of a fluid invading a heterogeneous media is an example of phenomena where the combination of theory, experiment, and numerical modeling can be used together to investigate a system in detail [3,11,14].

Few years ago, Pinto et al. [43] reported an amazing spontaneous pattern formation during the quasi-static grain–grain displacement in a Hele-Shaw cell, varying some of the grains characteristics. The patterns displayed beautiful fingered structures for some parameters combinations, and sometimes symmetric six-folded structures have emerged [43]. At that time, a simulation was performed and qualitatively validated by the experimental results, but several questions concerning the microscopic features of the simulation remained open. In this work, we hope to fill some of these gaps, presenting detailed results for the fingering phenomena in a radial Hele-Shaw geometry, varying the friction, stiffness constant, and the geometries of the grain assemblies. We also extended the original study to consider an axial geometry, the channel, in order to investigate the origins of the fingering formation in granular media and explore more closely the analogies with the Saffman–Taylor viscous fingering phenomena during the displacement of immiscible fluids [18,37,51].

Thus, after this brief introduction we present in the next section the basic methods used in the simulations and how to extract the measured quantities in each geometry. Next, we present our results considering the radial and axial geometries, closing the paper with our conclusions, acknowledgements, and the references.

2 Methods

The numerical simulations were performed using a code based on Discrete Element Method (DEM), developed by us in C language, dedicated to 2D circular shapes—disks. In this code, the motion of particles is time discretized by a 3^{rd} order Gear Predictor–Corrector scheme [1]. Our DEM code is, thus, an explicit time-iterative approach composed of three main numerical stages: *(i)* prediction of the grain's position, velocity, acceleration, in both in translation and rotation; *(ii)* detection of grains which are in contact and evaluation of the contact force; and *(iii)* correction of the grain's position, velocity, acceleration, in both on translation and rotation, with the use of the 3rd order Gear coefficients [1].

The rigid disks interact each other at the contact points, Fig. 1a. Each time that a contact occurs, the overlap distance $d_{ij} < 0$ between the two disks i and j is computed (Fig. 1b; $d_{ij} = \|\mathbf{r}_j - \mathbf{r}_i\| - R_i - R_j$, where $\mathbf{r}_i$ and $\mathbf{r}_j$ are the coordinates of the grains i, j, respectively; and R_i, R_j, their radii, respectively). The normal repulsive force $f_n > 0$ is hence computed and assumed proportional to d_{ij}; $f_n = -k_n\, d_{ij}$. k_n denotes the normal stiffness of the contact, Fig 1c. It is constant for all contacts involved in the simulation, no matter the radii of the two disks which are in contact. Since that adhesion forces are not taken into account in this work, f_n is always positive. In order to be able to reach equilibrium states, the internal energy of the system must be damped. One way is to consider inelastic shocks between particles.

For that, a viscous force is added to f_n; $f_n = -k_n\, d_{ij} - \eta_n\, \delta v_{ij}^n$, where δv_{ij}^n is the normal relative velocity in the contact between grain i and j. The damping coefficient (viscosity) is defined by $\eta_n = 2\zeta\sqrt{k_n\, m_{ij}}$ ($m_{ij} = \frac{m_i m_j}{m_i + m_j}$ is the reduced mass of the two grains i and j of mass m_i and m_j, respectively) where ζ is a non-dimensional parameter such that $\zeta = 1$ corresponds to the critical damping, i.e., perfectly inelastic shock. In order to ensure the numerical convergence of the discretized scheme of Newton's equations, ζ must be smaller than 1; we use $\zeta = 0.95$.

In each contact, friction is taken into account. Hence, a tangent force f_t is computed for each grain contact. The force model used for f_t is incremental and follows the one suggested by Cundall & Strack [21]: for each time step ΔT, an increment of tangential force opposed to the increment of the tangential relative displacement δU_t is computed, $\delta f_t^{\Delta T} = -k_t\, \delta U_t$. At time $T + \Delta T$, the total tangent force is thus given by $f_t = f_t^{T+\Delta T} = f_t^T + \delta f_t^{\Delta T}$. Hence, time step after time step, f_t is incremented or decremented. Nevertheless, f_t is limited by the Coulomb condition, $|f_t| \leq \mu f_n$, where μ is the static coefficient of friction between grains, Fig. 1d. The next stage consists in computing the sum of the forces on each grain (contact forces and volume forces, *e.g.*, the drag force due gravity acceleration), $\mathbf{F}_i$. The corrected acceleration is hence computed for each grain $\mathbf{a}_i^c = \mathbf{F}_i / m_i$.

Table 1 Parameters used in simulation, in normalized unities (see [8] for more details)

ΔT	k_n	k_t/k_n
10^{-4}	1000	0.75

The difference between the corrected acceleration computed at the end of the time step and the predicted acceleration evaluated at the start of the time step, $\mathbf{\Delta a_i}$, the so-called "corrector" is finally used with the Gear coefficient to compute the new velocities and new positions for the particles. This computation ends the current time step; grains are ready for a new time step. The explicit discretized scheme is conditionally numerically stable. To ensure that each time step will converge, one has to be sure that the time step ΔT used to numerically integrate the Newton's equations is smaller than the so-called critical time step $\Delta T_c = \sqrt{m_{ij}/k_n}$. ΔT_c corresponds to the typical contact duration when two particles shock each other. In order to accurately describe what happens since the contact creation to its end, the time step ΔT used in DEM must be only a part of ΔT_c. Depending on the accuracy required for the simulations, ΔT_c can be divided by 15, for raw descriptions of the contact physics, up to 100, for a very accurate computations of collisions. In this paper, we have arbitrarily used $\Delta T = \Delta T_c/50$ and the mass used to compute ΔT_c was the smaller mass present in the system, i.e., the mass of the smallest particle (Table 1).

For technical reasons, we chose the cross-sectional length of the system, L, as the unity of length. For other specific normalizations used in this code and for the values of the normalized elastic quantities, please check [8]. The normalization procedure applied here was designed to avoid large interpenetration of grains and save CPU time with unphysical calculations. All codes used here were developed by us in C language.

Thus, we are able to build different assemblies of grains and impose a variety of tests to them, changing geometries and microscopic parameters. From the positions, velocities, and forces of each element on the system, we can calculate strain and stress fields, and measure several quantities of interest, as the coordination number, response functions, elastic parameters, etc. [7,9,10,38].

In this work, we have particular interest in measuring the stress field for several different assemblies. Under very general considerations, it was shown [26] that an exact expression of the stress tensor $\sigma_{\alpha\beta}$ at position $\mathbf{r}$ for a static assembly of grains (i.e., when the kinetic part of the stress can be disregarded) is given by

$$\sigma_{\alpha\beta}(\mathbf{r}) = \frac{1}{2}\sum_{i,j;i\neq j} f_{ij\alpha} r_{ij\beta} \int_0^1 ds\, \Phi[\mathbf{r} - \mathbf{r}_i + s\mathbf{r}_{ij}]. \qquad (1)$$

In this expression, Roman indices are particles labels, whereas Greek ones denote the Cartesian coordinates. $\mathbf{r}_{ij} \equiv \mathbf{r}_i - \mathbf{r}_j$, are the branch vectors, where $\mathbf{r}_i$ is the center of mass of particle i, and $\mathbf{f}_{ij}$ is the force that the particle j applies over the particle i. The integral is performed along the direction of the contact, s (more details can be found in the chapter 14 of reference [42]). $\Phi(\mathbf{R})$ is an arbitrary coarse graining (CG) function which is normalized, positive semi-definite with a single peak at $\mathbf{R} = \mathbf{0}$, and a typical length w, the CG scale. In the case of a Gaussian CG function, as used here, this scale corresponds to the Gaussian width.

Note that the sign convention chosen here for the stress is the one commonly used for granular pressure (where compressive stress is positive), and not the one used in other fields of continuum mechanics (and in [26]). This expression for the stress obeys *exactly* the equation of static equilibrium $\partial_\beta \sigma_{\alpha\beta} = B_\alpha$ (the static limit of the momentum conservation equation), where B_α is the body force (e.g., $\mathbf{B} = \rho\mathbf{g}$ for packings of density ρ under gravity). Note that $\sigma_{\alpha\beta}$ depends, in general, on the choice of Φ, and in particular on the coarse graining scale. Continuum mechanics is based on the notion that there exists a range of values of w, sufficiently large compared to the microscopic scale, but smaller than the scale of the microscopic gradients (a scale separation regime), for which the macroscopic fields, such as the stress tensor, are independent of w and of Φ. The existence of such a regime in the systems was demonstrated in [23]. We have used a Gaussian coarse graining function, $\Phi(r) = \frac{1}{\pi w^2}\exp -(|r|^2/w^2)$, where w corresponds to the Gaussian width, and $w = 6d$, where d is the mean diameter of grains. Since that our simulations were performed on quasi-static regime (typical displacement imposed is $1/5000$ mean diameter by time step) the contact component contribution for the stress field is several orders of magnitude larger than the dynamical one, which justifies our choice to disregard the kinetic stress term.

Now we will present the different geometries used for the assemblies of grains, describing the particular choices made in each case. In general, we have considered three different assemblies of grains: monodisperse, bidisperse, and polydisperse. The *monodisperse* assembly considers exactly the same radius for all grains. In some cases we test displacement of a monodisperse assembly by another one with different radius, but if nothing is specified, assemblies with exactly same radii are used. The *bidisperse* assemblies have grains of two sizes, typically R and $R/2$, with the same amount of mass for each subset. In this way, the bidisperse assembly avoids crystallization more efficiently than any other assemblies—Fig. 2. The *polydisperse* assemblies consider a uniform distribution of radii in the range $R(1-\epsilon) < r_i < R(1+\epsilon)$. In this case, we can expect some segregation effects and also crystallization, but in much less extension compared with the monodisperse case. Figure 2 is a remarkable example where even a small amount of polydispersion ($\epsilon = 0.05$) can alter

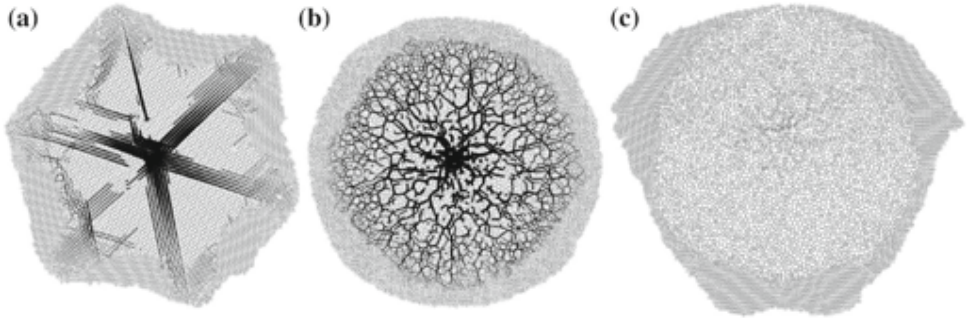

Fig. 2 Force chain network for different configurations in radial geometry. The three configurations are generated using DEM simulations with different assemblies of grains. **a** Monodisperse grains displaced by monodispersed ones. **b** Polydisperse substrate displaced by polydispersed grains. **c** Monodisperse base displaced by bidisperse assembly. Note that only with monodisperse assembly, the displacement results to a fingering pattern

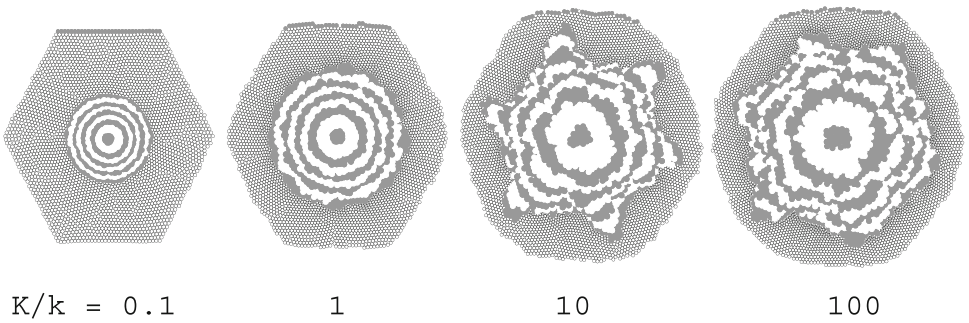

Fig. 3 Spontaneous pattern formation during grain–grain displacement. We show the pattern formation during the injection of monodisperse grains with radius $R = 1.5$, in a monodisperse substrate with radius $R = 1$. From *left* to *right*, the ratio of the normal stiffness constant to the injected grains relative to the displaced ones, K/k, is increased from 0.1 to 100. Clearly, for $K/k = 10$, the fingering formation is enhanced

dramatically the resulting pattern formed due the grain displacement.

2.1 Radial geometry

In this case, the system is equivalent to the experimental Hele-Shaw geometry [43]. A substrate consisting of grains placed in a hexagonal pattern, with plane symmetry and without gravity, is initially generated. Basically, the grains on the substrate occupy a triangular lattice (six next-neighbors) in such a way that they form an initial hexagonal pattern that will be deformed with the injection of the grains. Then, grains are inserted on the system from the center, one by one. The algorithm to insert a grain is a bit tricky. Basically, the grain is inserted in a random empty place found within a circle of radius $3d/2$ centered at the center of mass of the initial substrate. Initially, the inserted grain has its radius set to 0 and it grows at each time step by a ratio $d/10,000$. After 5000 steps, this increase of radius is stopped and the system is left to relax by another 5000 time steps. Thus, the grains are inserted in each 10,000 time steps, one by one.

Typically, a simulation run has 3781 grains in the substrate and another 3500 grains are inserted along the simulation. To avoid grain evasion and to mimic the effect of the glass plates of the Hele-Shaw apparatus, we introduced an additional viscous drag friction, ϑ. It simulates the loss energy between the grains and the cell plates and can assume values between 0 and 1, in analogy with "drag friction," $F_D = -bv_i$ where v_i is the velocity of the grain i and $b = \vartheta/(1-\vartheta)$. We fixed the value to $\vartheta = 0.1$ in all simulations shown here. The normal stiffness used on the inserted grains was 10 times greater than the value used on the grains of the base, since it was the value which has enhanced the fingers—Fig. 3.

Some parameters were varied in order to observe the collective behavior and determine which ones enhance the fingering pattern. In all cases considered here, the injected grains are larger than the displaced ones, since it was the case in which the experiments displayed fingered patterns. However, we also have obtained fingered formation using injected grains smaller than the displaced ones, since in simulations, the system is strictly two-dimensional, and, in the experiments, the spatial feature of the setup was the responsible to frustrate the fingering formation [43]. We generate

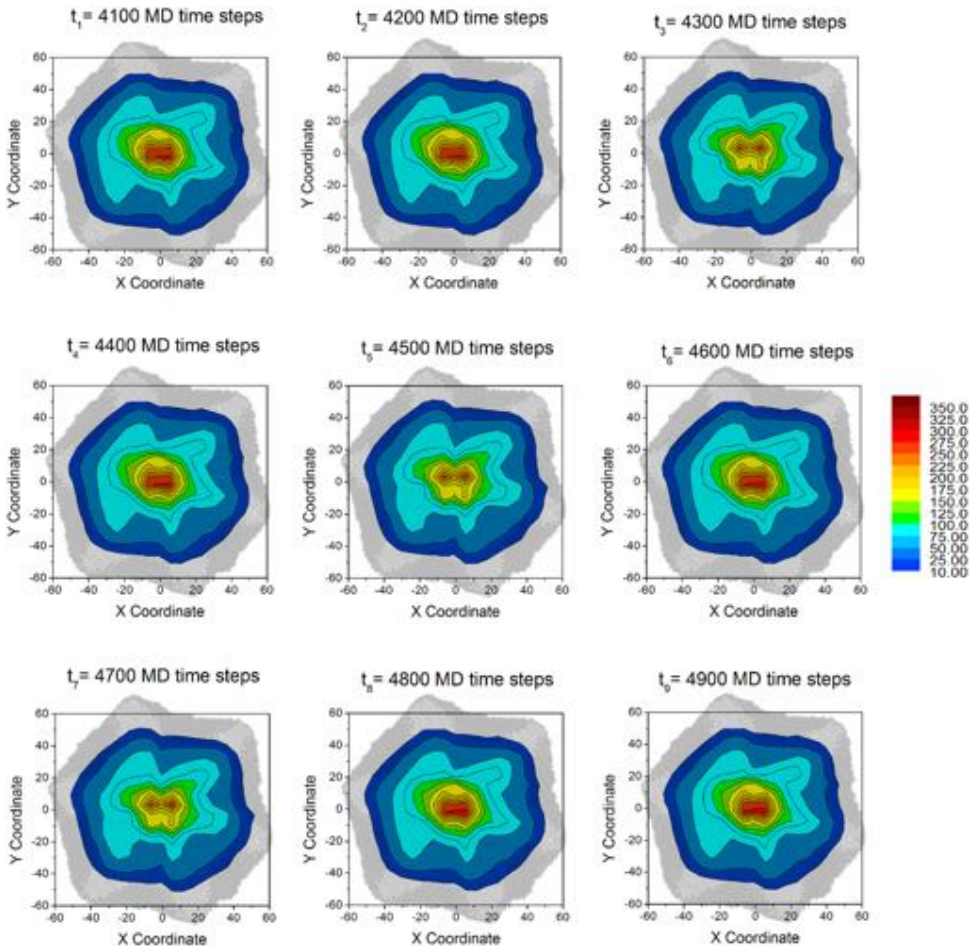

Fig. 4 Stress evolution of a monodisperse substrate during the insertion of a single grain. As explained in the text, each panel corresponds to the instantaneous stress field calculated after 100 time steps, during the last 1000 time steps of insertion of a grain. Note the heterogeneous feature of the stress field, with higher values along the fingers' directions. Time is increasing from *left* to *right* and from *top* to *bottom* as indicated

10 samples for each set of parameters. The friction coefficient was set to $\mu = 0.5$, unless explicitly indicated, and we have tested the following combinations of displaced/injected grains:

- *Monodisperse/monodisperse* different friction coefficients between particles were tested ($\mu = 0.10, 0.50, 0.90$);
- *Polydisperse/polydisperse* with polydispersion of 30% ($\epsilon = 0.3$);
- *Monodisperse/bidisperse* injected grains are bidisperse with radii ratio $R/r = 2/1.4$. Grains on the substrate have unitary radii;
- *Polydisperse/monodisperse* radii of injected grains 1.5 times larger than the size of the largest grain of the substrate.

In order to better understand the mechanism involved during the grain injection, we follow the stress field during the injection of a single grain in the first two combinations of geometries described above. To avoid transient effects, we calculate the stress along the insertion of the last grain in a sample of each system. The data were collected at each 100 time times steps and the instantaneous stress profiles are calculated from Eq. 1. These profiles are shown in Figs. 4 and 5 for 1000 time steps, allowing to observe the evolution of the stress profiles.

2.2 Axial geometry

We consider in this case a channel as shown in Fig. 6, filled typically with $N = 30,000$ grains of a given assembly. Connected to this channel, another channel, narrower, is filled with another set of grains (typically $N/8$ monodisperse grains) which are then pushed into the larger channel by a piston with constant velocity (in all simulations with this geometry, a displacement of $d/15,000$ is imposed at each time step). The grains are confined by lateral and top walls. The lateral walls are in general fixed but, eventually, a constant pressure is imposed to the walls to allow them to move. The top wall is placed atop the assembly of grains and it is free to move (it has a mass corresponding to that of 1000 average grains). Again, we have disregarded the gravity and considered $\vartheta = 0$ in this case. Thus, on this geometry, all the system parameters can be kept fixed and only the geometry of displaced assembly be varied, allowing to test the elastic and mechanical macroscopic properties of the specific geometry

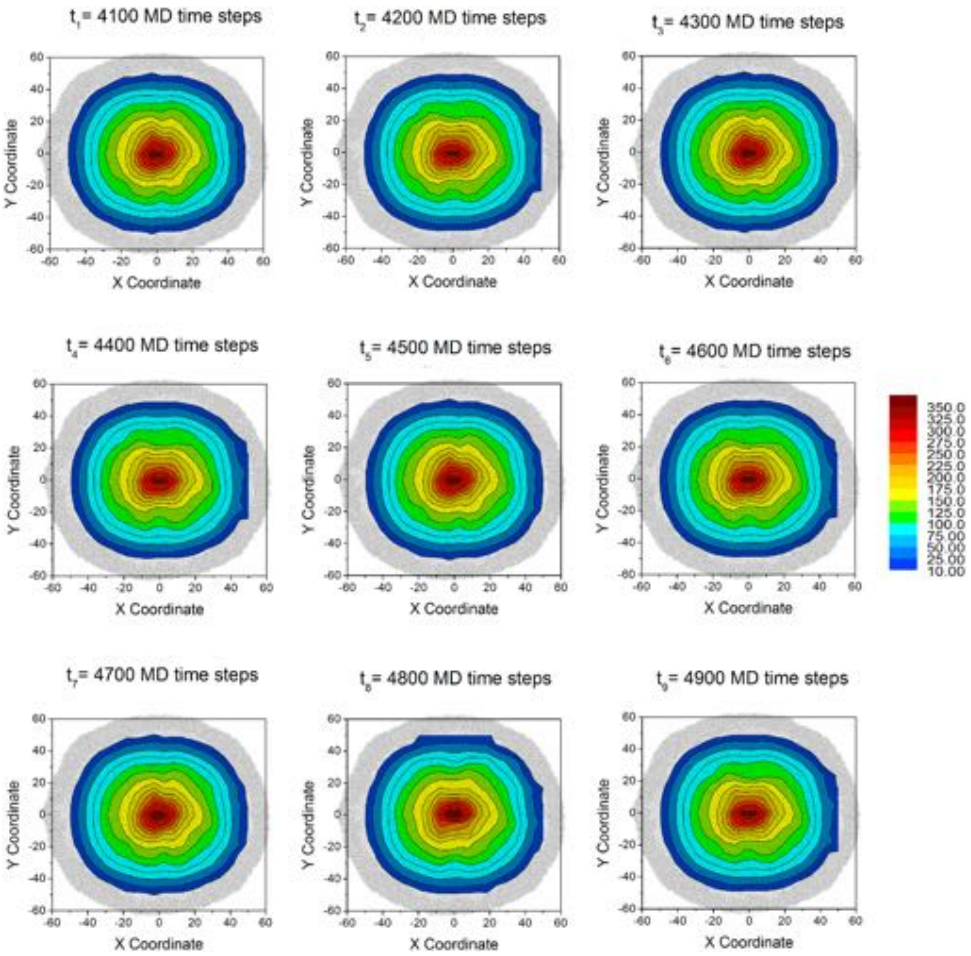

Fig. 5 Stress evolution when one grain is inserted into a polydisperse sample. In this case, the stress field is much more homogeneous than the monodisperse case. The sequence of images corresponds to the stress field fluctuations due the insertion of a single grain at each 100 time steps, during the last 1000 time steps of insertion of a grain. Time is increasing from *left* to *right* and from *top* to *bottom*

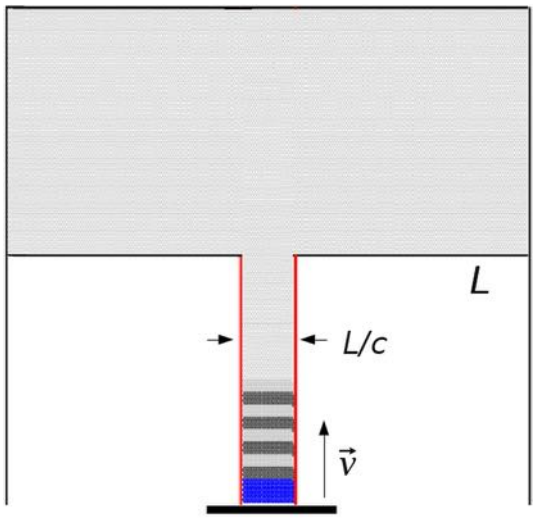

Fig. 6 Scheme used in the axial geometry. A channel filled with grains of a certain geometry is displaced by another set of grains pushed from a narrow channel with constant velocity v, with aid of a piston. The typical lateral extension of systems is $L = 240$ and the narrow channel has typically $1/10$ ($c = 10$) of the lateral extension. The last grains in the piston were *colored* in alternative layers to allow the observation of the deformation of the layers during the grain injection

considered. In order to explore the origins of the fluid-like behavior during grain–grain displacement, we decide indeed to keep all control parameters fixed (k_n, k_s, μ etc.), and to vary only the assembly geometries used in the large channel: monodisperse, bidisperse, and polydisperse (5 %). The set of injected grains are monodisperse in all the cases considered here in order to keep the loading of material exactly the same during the tests.

In this geometry, a direct comparison with the Saffman–Taylor experiment [51] is possible. The effective viscosity of the medium during the displacement of grains can be estimated from the stress tensor measured along the growing interface between inserted and displaced grains, as explained in the following paragraph.

Darcy flow Consider the flux Q of granular material along the channel. Defining ϕ as the packing fraction, the ratio of the total area of grains to the area of the channel, we can write the following expression for the discharge of material, Q,

$$Q = \phi \overline{v} \frac{L}{c}, \tag{2}$$

where $\overline{v}$ is the mean velocity of the injected material and L is the width of the channel. L/c corresponds to the width of the narrow channel used to inject the grains, and c is the reduction factor used in the narrower channel. Considering the Darcy law for viscous laminar flow in fluids,

$$Q = \frac{-\kappa A \nabla P}{\eta}, \tag{3}$$

where ∇P is the pressure gradient, κ is the permeability, and A is the cross-sectional area of the channel, we can write the following relation for the effective viscosity η_{ef},

$$\eta_{ef} = \frac{-c\kappa \nabla P}{\phi \overline{v}}. \tag{4}$$

Thus, by measuring the pressure drop along the displacement front of the injected material, and the stationary velocity of the front, we expect to be able to estimate an "effective viscosity" for the displacement of grains on each assembly studied. Since we consider the same geometry of the channel, it is reasonable suppose that the value of κ is constant for all simulations. ϕ and $\overline{v}$ are also kept constant, since the grains are injected exactly in the same way along the different experiments. Thus the only effect on the measured η_{ef} should be due the specific geometry used in the assembly of displaced grains.

3 Results and discussion

We present in this section our major findings concerning the fingering phenomena during the grain–grain displacement in the two geometries described above. First, we show the results for the radial geometry, inspired by the Hele-Shaw cell and the experimental setup [43]. After, we show the results for the axial case, which was designed for a more specific comparison of different assemblies of grains, and present a quantitative comparison of the effective viscosity measured to each assembly. The idea along the analysis presented is, starting with the simulation parameter set corresponding to the best reproduction of the experimental data, gradually sweeps the parameter space varying microscopic features of the grains and also the assembly geometry to explore the fingering formation. Next, with the axial geometry, we reduce the complexity of the system to the minimal, in order to systematically test the analogy with the immiscible fluid displacement—Saffman–Taylor fingering phenomena.

3.1 Radial geometry

Here, we show results for the displacement of different combinations of injected/displaced geometries, as well for different sets of the microscopic control parameters in order to explore the parameter space of the system. In previous work [43], the authors presented results from several experiments of injection of grains in a Hele-Shaw cell, varying the type of grains (steel, plastic, styrofoam) and their relative sizes and geometries. They show that when a monodisperse assembly of grains is injected, with larger diameters compared to the displaced ones, there is a tendency to spontaneous fingers' formation, especially six-fingered patterns.

In the original work, the friction coefficient between particles was fixed to $\mu = 0.5$. Thus, we decided to vary it to determine its physical influence in the collective behavior of grains. The substrate assembly was also tested for monodisperse and polydisperse ones. For each case tested, 10 samples were generated in order to observe stochastic fluctuations. Some of results are shown in Fig. 7, where the thickness of the black lines corresponds to the contact force magnitude between grains. It is possible to infer that the geometry of the displaced grains has almost no influence in the pattern formation based on the tests with monodispersed (triangular and square lattices), bidispersed, and polydispersed grains. The only difference observed was some irregularities in the boundaries between the inserted grains in the polydispersed substrate case. The stress on the system increases with friction, as noted in the force chain magnitude in Fig. 7, and we have confirmed that the value $\mu = 0.5$ enhances the formation of the six-folded pattern, but for all friction coefficients tested, there was spontaneous fingering formation. Since the elastic modulus of the inserted grains was kept fixed to 10 times the modulus of the displaced grains, as already explained in the Sect. 2, we can conclude that the friction coefficient between grains does neither play a central role on the fingered pattern formation nor on the substrate geometry.

Figure 2 shows the contact force chain network for three different samples. Here, only contacts in which the force magnitudes are larger than the local mean forces are shown. As the grains are pushed from the center, it is natural to infer that the intensity of the forces will decrease radially from the middle. Thus, we determine the average local force along radial direction to allow the comparison with the intensity of the contact forces which are at the same distance from the center. In the monodisperse configuration, the force chains are clearly along the fingers' directions. In the polydisperse systems, the force chains directions seem to be random, feature which is enhanced for the bidisperse system. All the polydisperse samples resulted in symmetrical hexagonal patterns, with some fluctuations, and all the bidisperse systems resulted in more smooth circular shapes. However, the substrate displaced by the bidisperse systems displayed irregular shapes differently to the circular patterns displayed in the polydisperse substrate samples. It occurs due the crystallization which develops spontaneously in the monodisperse case.

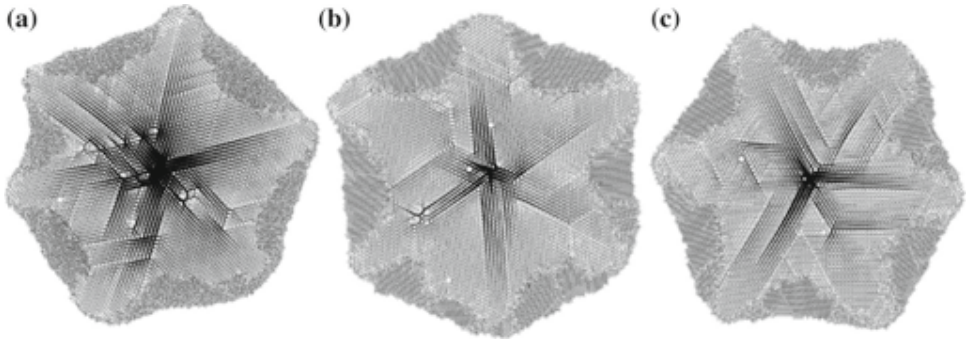

Fig. 7 Monodisperse inserted grains with different friction coefficients between particles. **a** Polydisperse substrate (30 %), with monodisperse injected grains. Friction coefficient between particles equals to 0.5. **b** Monodisperse base and monodisperse injected grains with friction coefficient between particles equal to 0.1. **c** Monodisperse configuration (base and injected grains) with friction coefficient equals to 0.9. Note that in **a** we can clearly observe the force chains oriented to the fingers, as well the increase of stress on the tips

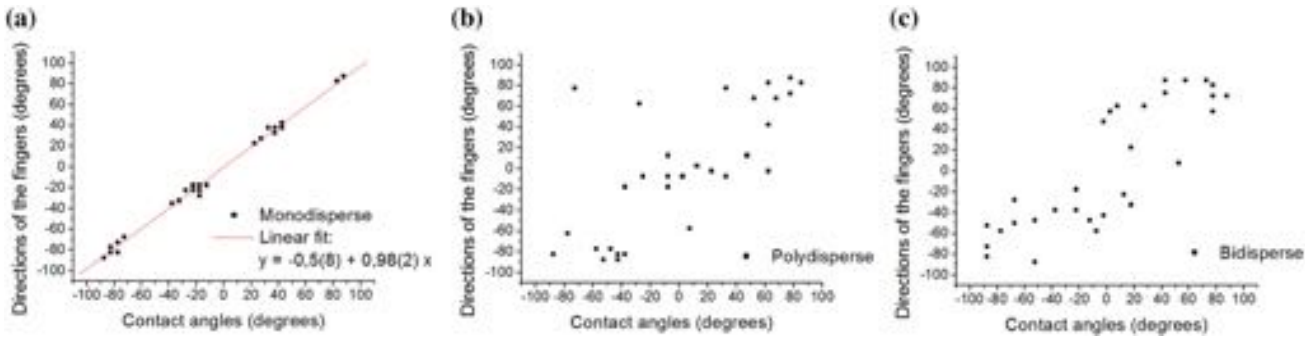

Fig. 8 Correlation between the three preferential directions of the contact vectors along the direction of the fingers and the three most frequent contact angles from force contact network. **a** Monodisperse system. **b** Polydisperse system. **c** Bidisperse system. For monodisperse configuration, we expected that the points would be distributed in a linear function with slope equal to 1.0, and the results obtained of the linear fit were $Y = -0.5(8) + 0.98(2) \times$ with $R = 0.997$, corroborating our prediction. This plot represents a quantitative result showing that the contact angles are in the fingers' directions. For polydisperse and bidisperse configurations, it was expected no correlations between the three peaks and the contact angles, which is confirmed by the sparse cloud of points obtained in these cases

To test the qualitative conjecture that the principal contact direction of monodisperse systems is responsible for the finger formation [43], we performed a quantitative verification of this conjecture. In the case of the polydisperse and bidisperse systems, we expect that the contact angles are not in the same direction of the largest concentration of injected grains (fingers). To prove it, three graphs were generated, for each configuration tested, as shown in Fig. 8. Here, the correlation between the main directions of the fingers measured on the samples and the most frequent contact angles on these samples are shown. Clearly, for the monodisperse case, a very strong correlation is observed, while for the other cases we do not observe any clear correlation.

Thus, we can assure that the fingering pattern formation is associated with the crystallization of the inserted grains, as conjectured by Pinto et al. [43]. The resulting hexagonal pattern should be related to the spontaneous hexagonal lattice which is formed when monodisperse grains are confined (one grain has, in general, contacts with six neighbors which can open or close randomly). It interesting to note that this configuration is the one which have the smallest relation between the perimeter and the occupied area, as known by the bees which build their honeycombs in hexagonal lattices [29]. In a confined system, the grains are distributed in a close-packed configuration, thus they tend to form regular structures and then crystallize. In a crystallized sample, when one grain receives a force coming from a neighbor grain, the force chain can propagate along the radial direction, or can split in two, generally with an angle of 60°, between two of the opposing neighbors of the grain; the grains will move in the force directions, and, considering the symmetry of the neighborhood, it will imply to the six fingering pattern observed in the experiments and simulations. In polydisperse and bidisperse systems, crystallization is frustrated due the size dispersion on these systems: when a grain receives a force from a contact, there is no preferential direction to propagate the stress, leading to the circular deformed patterns observed.

Figures 4 and 5 show, respectively, the stress evolution for monodisperse and polydisperse simulations. The instantaneous stress profiles were generated to observe the

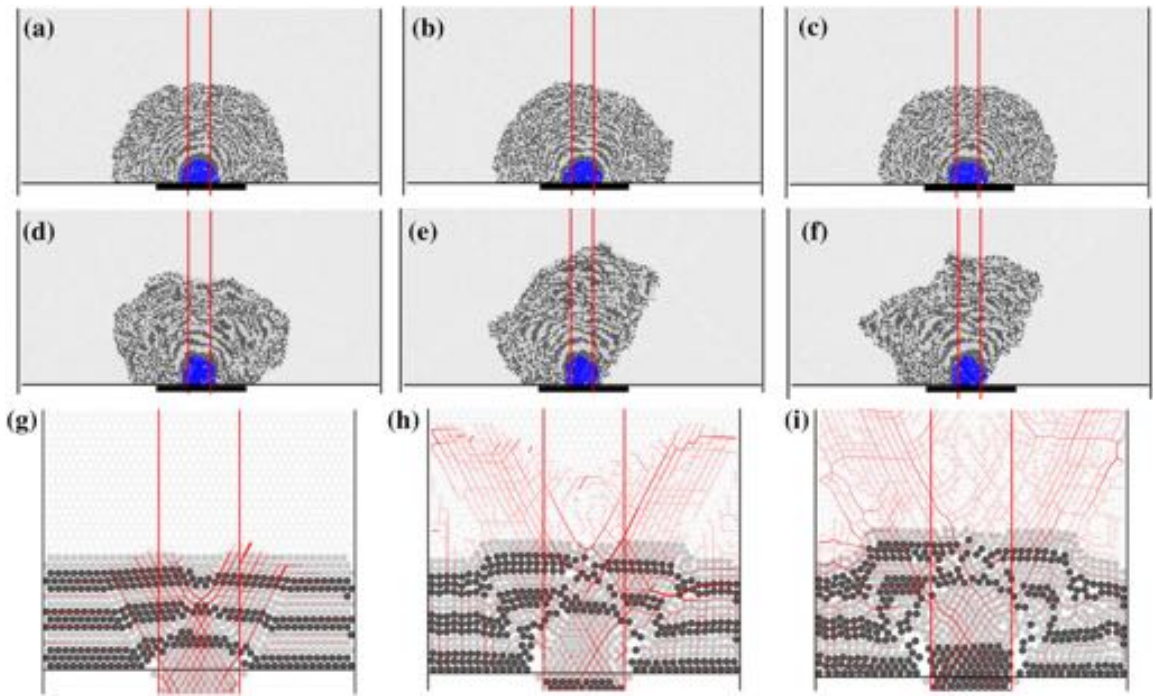

Fig. 9 Morphologies obtained for the case of the axial geometry. In all cases, a monodisperse set of grains is injected on the substrate. In the *first row* (**a**–**c**), three samples with a bidisperse substrate; in the *second row* (**d**–**f**), three samples with pattern formation in a polydisperse (5 %) substrate. Note the difference between the "wetting" angle of the interface formed by the injected/displaced grains. The *bottom row* (**g**–**i**) the injection into a monodisperse substrate is shown. In this case, the *panels* show the temporal evolution of the injected grains, the time increases from **g** to **i**. The *red lines* between grains denote the contact forces. Note the elliptic-like force propagation along the system. A zoom of the injection area is shown to enhance the visualization. (Color figure online)

stress evolution during the insertion of a single grain. In the monodisperse case, we observe the heterogeneity of the stress field, particularly the stress enhancement along the fingers' directions. The stress magnitude is larger in the center because the grains are pushed from there, but we can observe a kind of compression/decompression cycles. These cycles could be associated to the sound propagation along the sample, reflecting on the borders and coming back with a period of around 200 time steps; thus, several cycles occur during the injection of a single grain that takes 5000 time steps to be concluded. In future works, we plan to address this observation in a more detailed manner. The stress seems to propagate from the center along two preferential directions. These results agree with the hyperbolic models of stress propagation in anisotropic granular systems [24,25]. The instantaneous stress profiles of the polydispersed sample have a circular pattern, with no preferential direction, but the system works similarly as the monodisperse cases: in cycles of compression/decompression where the stress in the center increases and relaxes but alternates in random directions. In this case, the stress propagation approaches to the predicted by the diffusive models of stress propagation in isotropic granular assemblies, showing a transition from the center to the borders of the pattern.

3.2 Axial geometry

As already mentioned, we considered the axial geometry (Fig. 6) with different assemblies of grains in the large channel: monodisperse, bidisperse, and polydisperse (5 % dispersion). The injected grains are always of same type, monodisperse. In Fig. 9, we show results for the interfaces obtained using different assemblies of grains. It is interesting to note that when the displacement assembly of grains used was bidisperse, a symmetric diffusive-like pattern arose, and tiny fluctuations were observed between the samples (here we show results from five different samples of each preparation). The "wetting angle" (angle formed by the internal tangent of the interface and the wall) is $\theta_b < 90$, indicating, on this analogy, the displacement of a more viscous fluid into a less viscous one. If we consider now the results for the polydisperse case, it is clear that a wetting angle $\theta_p > 90$ is observed in all samples displayed, even that in this case the interfaces are much more fluctuating. The analogy with the fluid displacement clearly indicates the displacement of a more viscous fluid displaced by a less viscous one. When monodisperse assemblies are used, the profiles obtained are analogous to the polydisperse case but, as shown in the panel C of Fig. 9, in this case a strong elliptic-like propa-

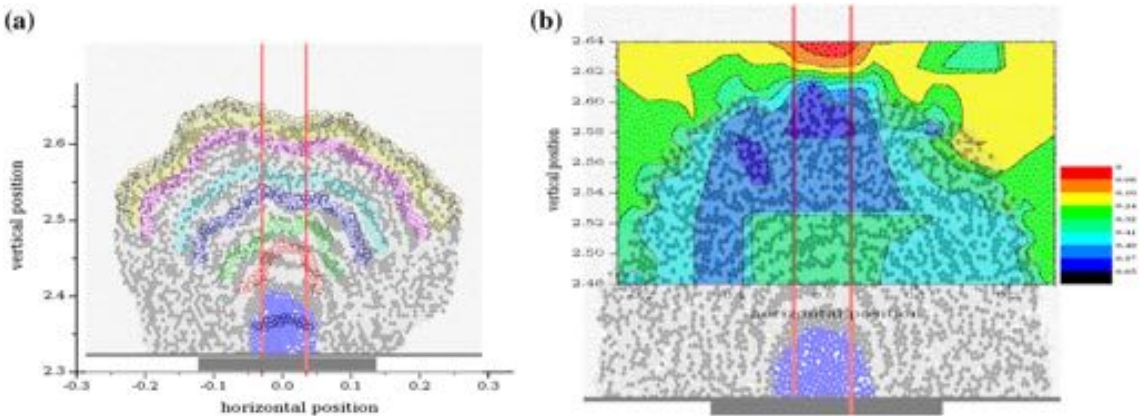

Fig. 10 **a** Profiles obtained along the displacement of the grains. We show the grains considered as the front interface during the displacement of a polydisperse sample. The pressure gradient is measured taking the difference between the average stress calculated along the interface in function of time. **b** Stress field obtained for a given interface in a bidisperse sample. Note the gradient of stress along the interface. In this case, we never observe fingers

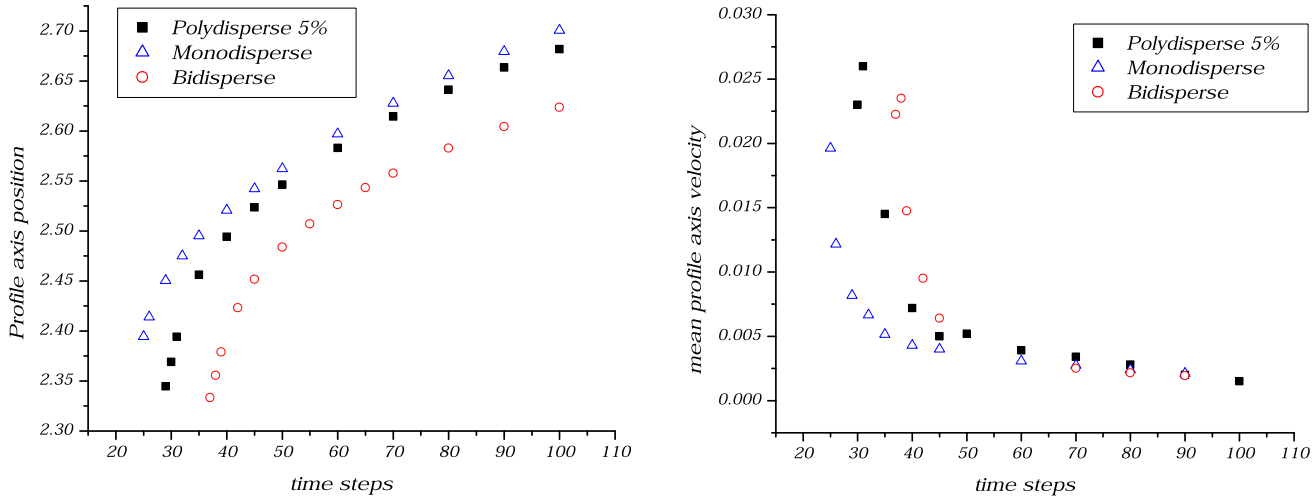

Fig. 11 *Left* Evolution of the interface axis position with time for the three different assemblies considered. The results represent average over five samples. *Right* corresponding velocity profiles for the same assemblies

gation of forces is observed, leading to finger formation due the displacement on preferential directions. This preferential displacement implies that some regions of the substrate remain stagnated, leading to high heterogeneity on the force chains—Fig. 9 and stress fields—Fig. 10.

In order to quantify the viscosity of the displaced medium, and following the reasoning presented in the Sect. 2, we measured the stress field from the contact network using Eq. 1, as shown in Fig. 10. We show in the left panel the grains considered as the interface for several instants of time. Then, we measured the stress field along the interface, as shown in the right panel, and its mean value is used to calculate the pressure gradient—Eq. 4. The pressure is calculated as the sum of the trace of the stress matrix, $\sigma_{nn} + \sigma_{tt}$, where n and t are the normal and tangential directions, respectively. This value is averaged along the interface between injected/displaced grains, and the stress gradient is computed as the difference between the value of the mean pressure at the time t and the pressure at the beginning of the injection, $t = 0$, divided by the mean radius of the interface. In order to calculate the effective viscosity, we need to compute the mean position of the interface, as shown in Fig. 11. We also show the results for the mean velocity for all assemblies considered. In all samples considered here we used the same microscopic parameters, the only variation was in the assembly geometry used in the displaced substrate, which can be then associated with the effective viscosity measured.

Finally, we are now able to compute the effective viscosity for each granular assembly. The results shown in Fig. 12 confirm our expectations, but only partially. As we can observe in this figure, the bidisperse assembly presented the lowest value for the effective viscosity, confirming its role as the less viscous fluid from the previous analysis based only on the pattern formation. However, for our surprise, the polydisperse

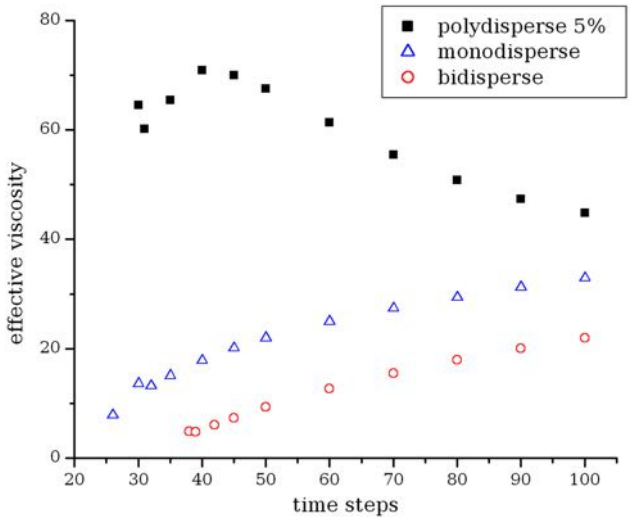

Fig. 12 Effective viscosity for different granular assemblies. From Eq. 3 we are able to estimate the effective viscosity for a given assembly. The bidisperse case displays the lower effective viscosity opposing to the polydisperse case

assembly presented the largest values for the effective viscosity. And, differently to the mono and bidisperse assemblies which became stiffer with time, analogously to the dilatant regime for sheared fluids, the effective viscosity of the polydisperse assembly has *decreased* with time, analogously to a shear thinning fluid. This behavior is rather unexpected for granular assemblies, since we expect that the increasing of the contact network would lead to a hardening of the material. However, for polydisperse assembly, we observe the contrary, a thinning of the system with time. Despite we do not have a definitive explanation for this behavior, we believe that it is linked with the fact that the force chains are short ranged in time and space; so, after an initial hardening when the force chains are initially formed, after a while, they became broken leading to the decreasing of the medium resistance. It interesting to note that all curves seem to converge to the same asymptotic value; it is reasonable to expect once that, as the time evolves, the injected grains will occupy the place of the displaced grains; as the injected assembly used is the same for all cases, we should expect that, asymptotically all systems will behave analogously.

4 Conclusions

We report spontaneous pattern formation during the displacement of grains considering different geometries and assemblies of grains. We confirm previous conjectures regarding analogies between the displacement of grains and the Saffman–Taylor fingering phenomena in immiscible fluids, showing that the fingers develop along preferential directions where the stress tensor is locally higher. Besides, using a channel geometry, we are able to measure an effective viscosity for granular assemblies, confirming that the monodisperse case corresponds to a "more" viscous fluid compared to the bidisperse assembly as the "less" viscous fluid. However, the results for the effective viscosity for the polydisperse case were very surprising for us, and we cannot furnish a satisfactory explanation at this moment. To our knowledge, this was the first measure of this type applied to granular assemblies and it opens new possibilities to explore the analogies between the displacement of immiscible fluids and granular materials. We expect to perform analogous measures using different kinds of assemblies in order to systematically test the procedure to quantify the effective viscosity. Another defying perspective on this work is to perform the injection using 3D assemblies, which could be particularly interesting for applications in nature and industry, as oil extraction [52].

Acknowledgments We are indebted to E. Clèment and P. Claudin for fruitful discussions. APFA thanks FAPEMIG and CNPq funding brazilian agencies. NMPM thanks CAPES for funding and CEFET-MG and 3S-R Laboratory for the kind support for academic interchange. We thank the anonymous referees for the very detailed and constructive reports of our manuscript.

Funding This study was funded by brazilian agencies CNPq and FAPEMIG.

Compliance with ethical standards

Conflict of interest The authors declare that they have no conflict of interest.

References

1. Allen P, Tildesley D (1987) Computer simulation of liquids. Oxford University Press, Clarendon
2. Alonso-Marroquín F, Herrmann HJ (2004) Ratcheting of granular materials. Phys Rev Lett 92:054,301
3. Amaral LAN, Barabási AL, Stanley HE (1994) Universality classes for interface growth with quenched disorder. Phys Rev Lett 73:62–65
4. Andreotti B, Forterre Y, Pouliquen O (2013) Granular media: between fluid and solid. Cambridge University Press, Cambridge
5. Aranson I, Tsimring L (2006) Patterns and collective behavior in granular media: theoretical concepts. Rev Mod Phys 78(2):641–692
6. Atman APF, Brunet P, Geng J, Reydellet G, Claudin P, Behringer RP, Clément E (2005) From the stress response function (back) to the sand pile "dip". Eur. Phys. J. E 17:93–100
7. Atman APF, Brunet P, Geng J, Reydellet G, Combe G, Claudin P, Behringer RP, Clément E (2005) Sensitivity of the stress response function to packing preparation. J Phys 17(24):S2391
8. Atman APF, Claudin P, Combe G (2009) Departure from elasticity in granular layers: investigation of a crossover overload force. Comput Phys Commun 180(4):612–615
9. Atman APF, Claudin P, Combe G, Mari R (2013) Mechanical response of an inclined frictional granular layer approaching unjamming. EPL (Europhys Lett) 101(4):44,006

10. Atman APF, Claudin P, Combe G, Martins G (2014) Mechanical properties of inclined frictional granular layers. Granular Matter 16(2):193–201
11. Atman APF, Combe G, Ferreira TR, Barros JA (2013) Pattern formation during capillary rising of a fluid front into a granular media. In: POWDERS AND GRAINS 2013: Proceedings of the 7th international conference on micromechanics of granular media, AIP Conference Proceedings, vol. 1542, pp 1075–1078
12. Atman APF, Kolb E, Combe G, Paiva HA, Martins GHB (2013) Non-gaussian behavior in jamming/unjamming transition in dense granular materials. In: POWDERS AND GRAINS 2013: proceedings of the 7th international conference on micromechanics of granular media, AIP Conference Proceedings, vol. 1542, pp 381–384
13. Bak P (2013) How nature works: the science of self-organized criticality. Springer, New York
14. Barabási AL, Stanley H (1995) Fractal concepts in surface growth. Cambridge University Press, Cambridge
15. Caballero G, Kolb E, Lindner A, Cviklinski J, Lanuza J, Clément E (2005) Experimental investigation of granular dynamics close to the jamming transition. J Phys 17:S2503
16. Cates ME, Wittmer JP, Bouchaud JP, Claudin P (1998) Jamming, force chains, and fragile matter. Phys Rev Lett 81:1841–1844
17. Cheng X, Xu L, Patterson A, Jaeger Jaeger HMNSR (2008) Towards the zero-surface-tension limit in granular fingering instability. Nat Phys 4:234–237
18. Chevalier C, Ben Amar M, Bonn D, Lindner A (2006) Inertial effects on saffmantaylor viscous fingering. J Fluid Mech 552:83–97
19. Combe G, Richefeu V, Stasiak M, Atman APF (2015) Experimental validation of a nonextensive scaling law in confined granular media. Phys Rev Lett 115:238,301
20. Combe G, Richefeu V, Viggiani G, Hall SA, Tengattini A, Atman APF (2013) Experimental evidence of "granulence". In: Yu A, Dong K, Yang R, Luding S (eds.) POWDERS AND GRAINS 2013: proceedings of the 7th international conference on micromechanics of granular media, AIP Conference Proceedings, vol. 1542, pp 453–456
21. Cundall PA, Strack DLO (1979) A discrete numerical model for granular assemblies. Geotechnique 29(1):47–65
22. Duran J, Reisinger A, de Gennes P (1999) Sands, powders, and grains: an introduction to the physics of granular materials. partially ordered systems. Springer, New York
23. Goldenberg C, Atman APF, Claudin P, Combe G, Goldhirsch I (2006) Scale separation in granular packings: stress plateaus and fluctuations. Phys Rev Lett 96(16):168001
24. Goldenberg C, Goldhirsch I (2002) Force chains, microelasticity, and macroelasticity. Phys Rev Lett 89(8):084,302
25. Goldenberg C, Goldhirsch I (2005) Friction enhances elasticity in granular solids. Nature 435(7039):188–191
26. Goldhirsch I, Goldenberg C (2002) On the microscopic foundations of elasticity. Eur Phys J l E 9:245–251
27. Gutiérrez G, Colonnello C, Boltenhagen P, Darias JR, Peralta-Fabi R, Brau F, Clément E (2015) Silo collapse under granular discharge. Phys Rev Lett 114:018,001
28. Gutiérrez G, Pozo O, Reyes LI, V RP, Drake JF, Ott E (2004) Simple model for reverse buoyancy in a vibrated granular system. EPL (Europhys Lett) 67(3):369
29. Hales TC (2001) The honeycomb conjecture. Discrete Comput Geom 25(1):1–22
30. Herrmann H, Hovi J, Luding S (2013) Physics of dry granular media. Nato Science Series E. Springer, Dordrecht
31. Hinrichsen H, Wolf D (2004) The physics of granular media. Wiley, Berlin
32. Jaeger HM, Nagel SR (1992) Physics of the granular state. Science 255:1523–1531
33. Jaeger HM, Nagel SR, Behringer RP (1996) Granular solids, liquids, and gases. Rev Mod Phys 68:1259–1273
34. Johnsen O, Toussaint R, Måløy KJ, Flekkøy EG (2006) Pattern formation during air injection into granular materials confined in a circular hele-shaw cell. Phys Rev E 74:011,301
35. Kolb E, Cviklinski J, Lanuza J, Claudin P, Clément E (2004) Reorganization of a dense granular assembly: the unjamming response function. Phys Rev E 69:031,306
36. Lindner A, Coussot P, Bonn D (2000) Viscous fingering in a yield stress fluid. Phys Rev Lett 85:314–317
37. Lindner A, Derks D, Shelley MJ (2005) Stretch flow of thin layers of newtonian liquids: fingering patterns and lifting forces. Phys Fluids 17(7):072107
38. Magalhães CFM, Moreira JG, Atman APF (2010) Catastrophic regime in the discharge of a granular pile. Phys Rev E 82:051,303
39. Magalhaes CFM, Atman APF, Combe G, Moreira JG (2014) Jamming transition in a two-dimensional open granular pile with rolling resistance. Pap Phys 6:0–0
40. Makse H, Havlin S, King P, Stanley H (1997) Spontaneous stratification in granular mixtures. Nature 386(6623):379–382
41. Makse HA (1997) Stratification instability in granular flows. Phys Rev E 56:7008–7016
42. Mehta A (2007) Granular physics. Cambridge University Press, Cambridge
43. Pinto SF, Couto MS, Atman APF, Alves SG, Bernardes AT, de Resende HFV, Souza EC (2007) Granular fingers on jammed systems: New fluidlike patterns arising in grain–grain invasion experiments. Phys Rev Lett 99(6):068001
44. Pöschel T, Herrmann HJ (1995) Size segregation and convection. EPL (Europhys Lett) 29(2):123
45. Pöschel T, Luding S (2001) Granular gases. Lecture notes in physics. Springer, Berlin
46. Radjai F, Roux S (2002) Turbulentlike fluctuations in quasistatic flow of granular media. Phys Rev Lett 89:064,302
47. Ramos O, Altshuler E, Måløy KJ (2009) Avalanche prediction in a self-organized pile of beads. Phys Rev Lett 102:078,701
48. Richefeu V, Combe G, Viggiani C (2012) An experimental assessment if displacements fluctuations in a 2d granular material subject to shear. Géotechnique Lett 2:113–118
49. Ristow G (2000) Pattern formation in granular materials. Springer, Berlin
50. Rosato A, Strandburg KJ, Prinz F, Swendsen RH (1987) Why the brazil nuts are on top: size segregation of particulate matter by shaking. Phys Rev Lett 58:1038–1040
51. Saffman PG, Taylor G (1958) The penetration of a fluid into a porous medium or hele-shaw cell containing a more viscous liquid. Proc R Soc Lond A 245(1242):312–329
52. Sahini M, Sahimi M (1994) Applications of percolation theory. Taylor & Francis, London
53. Song C, Wang P, Makse HA (2008) A phase diagram for jammed matter. Nature 453:629–632
54. Thompson D (1942) On growth and form. No. v. 1 in Dover books on biology series. Dover, New York
55. Umbanhowar PB, Melo F, Swinney HL (1996) Localized excitations in a vertically vibrated granular layer. Nature 382:793–796
56. Vicsek T (1992) Fractal growth phenomena. World Scientific, Singapore
57. Zuriguel I, Garcimartín A, Maza D, Pugnaloni LA, Pastor JM (2005) Jamming during the discharge of granular matter from a silo. Phys Rev E 71(051):303
58. Zuriguel I, Janda A, Garcimartín A, Lozano C, Arévalo R, Maza D (2011) Silo clogging reduction by the presence of an obstacle. Phys Rev Lett 107:278,001